Modeling diurnal and annual ethylene generation from solar-driven electrochemical CO2 reduction devices

Journal:	*Energy & Environmental Science*
Manuscript ID	EE-ART-02-2024-000545
Article Type:	Paper
Date Submitted by the Author:	03-Feb-2024
Complete List of Authors:	Yap, Kyra; Stanford University, Chemical Engineering; SLAC, SUNCAT Center for Interface Science and Catalysis Wei, William; UC Berkeley, Chemical Engineering Rodríguez Pabón, Melanie; Stanford University, Chemical Engineering King, Alex; University of California Berkeley, Chemical and Biomolecular Engineering; Lawrence Berkeley National Laboratory, Liquid Sunlight Alliance Bui, Justin; Lawrence Berkeley National Laboratory, Joint Center for Artificial Photosynthesis; University of California Berkeley, Wei, Lingze; Stanford University, Chemical Engineering Lee, Sang-Won; Stanford University Weber, Adam; Lawrence Berkeley National Laboratory, Energy Technologies Area Bell, Alexis; University of California, Chemical and Biomolecular Engineering Nielander, Adam; SLAC National Accelerator Laboratory, SUNCAT Center for Interface Science and Catalysis Jaramillo, Thomas; Stanford University, Assistant Professor of Chemical Engineering

Broader Context

Increasing greenhouse gas emissions requires the discovery and development of technologies capable of both removing CO_2 and displacing current emissions-heavy technologies. Integrated solar fuels devices for CO_2 reduction (CO_2R) is a net-negative technology capable of converting waste CO_2 streams into valuable chemical commodities. Streamlining the scaling process of these technologies will require tools and methodologies that can bridge the gap between bench-scale experimental results and large-scale operating systems. A key challenge for the operation of integrated solar fuels devices is maintaining optimal selectivity profiles under conditions of diurnal (e.g., throughout the day) and annual irradiance. Herein, we present a model which combines experimental CO_2R results, local meteorological data, and computational methods to develop a temperature and dependent diurnal and annual model of gaseous product output to streamline the co-design of large-scale, integrated solar-driven CO_2R systems.

Modeling diurnal and annual ethylene generation from solar-driven electrochemical CO₂ reduction devices

Kyra M. K. Yap[1,2,‡], William J. Wei[3,4,‡], Melanie Rodríguez Pabón[1,2], Alex J. King[3,4], Justin C. Bui[3,4], Lingze Wei[1,2], Sang-Won Lee[1,2], Adam Z. Weber[4,*], Alexis T. Bell[3,4,*], Adam C. Nielander[2,*], Thomas F. Jaramillo[1,2,*]

[1]Department of Chemical Engineering, Stanford University, Stanford, CA 94305, United States

[2]SUNCAT Center for Interface Science and Catalysis, SLAC National Accelerator Laboratory, 2575 Sand Hill Road, Menlo Park, CA 94025, United States

[3]Department of Chemical and Biomolecular Engineering, University of California, Berkeley, South Dr., Berkeley, CA, 94720, United States

[4]Liquid Sunlight Alliance, Lawrence Berkeley National Laboratory, 1 Cyclotron Rd., Building 30, Berkeley, CA, 94720, United States

[‡]Authors contributed equally

*Corresponding authors

Adam Z. Weber: azweber@lbl.gov

Alexis T. Bell: alexbell@berkeley.edu

Adam C. Nielander: anieland@slac.stanford.edu

Thomas F. Jaramillo: jaramillo@stanford.edu

1

Abstract

Integrated solar fuels devices for CO_2 reduction (CO_2R) are a promising technology class towards achieving net-negative carbon emissions. Designing integrated CO_2R solar fuels devices requires careful co-design of electrochemical and photovoltaic components as well as consideration of the diurnal and seasonal effects of solar irradiance, temperature, and other meteorological factors expected for 'on-sun' deployment. Using a photovoltaic-electrochemical (PV-EC) platform, we developed a temperature and potential-dependent diurnal and annual model using experimental CO_2R performance of Cu-based electrocatalysts, local meteorological data from the National Solar Radiation Database (NSRD), and modeled performance of commercial c-Si PVs. We simulated diurnal product outputs with and without the effects of ambient temperature to determine gaseous product temperature sensitivity. From these outputs, we observed seasonal variation in gaseous product generation, with up to two-fold increases in ethylene productivity between the Winter and Summer, analyzed the consequences of dynamic cloud coverage, and identified periods where device cooling/heating mechanisms could be implemented to maximize ethylene generation. Finally, we modeled the annual ethylene generation for a scaled 1 MW solar farm at three different locations (Beijing, CN; Sydney, AUS; Barstow, CA) to determine the consequences of local meteorological climates on PV-EC CO_2R product output, recording a maximum ethylene output of 18.5 tonne/yr at Barstow. Overall, this model presents a critical tool for streamlining the translation of experimental solar-driven electrochemical research to real-world implementation.

Introduction

Tackling climate change requires commercializing net carbon negative technologies capable of converting waste CO_2 streams into valuable, multi-carbon fuels and chemicals using solar energy as the driving force. For emerging technologies, like integrated solar fuels devices for CO_2 reduction (CO_2R), there is a need to develop tools and methodologies that can translate bench-scale experimental results to larger, pilot-scale on-sun operating systems. Successful scaling of integrated solar fuels CO_2R technologies represents an opportunity to significantly reduce greenhouse gas emissions and to enable decentralization and off-grid operation of chemicals production[1–3], allowing for flexibility in device location either close to the source of CO_2 generation or at the point of product consumption. Such flexibility could remove the need for long-haul chemicals transportation and the associated greenhouse gas emissions.[4–7]

A key challenge for integrated, on-sun solar-driven CO_2R is promoting selective multi-carbon product generation throughout the diurnal operation cycle (i.e., throughout the day). These selectivity profiles are a complex function of operating parameters such as voltage, current density, and temperature. Copper is the most widely studied electrocatalyst for multi-carbon product generation from CO_2R. However, it can produce up to 16 carbon products at a single potential, and small changes in the cathode potential can cause significant changes in reaction selectivity; for example, the Faradaic efficiency (FE) to C_2H_4 has been shown to vary by more than 10% with cathode potential changes of ~50 mV.[8–12] Additionally, electrocatalyst properties, such as catalyst morphology, loading, and composition as well as microenvironment effects including pH, temperature, and mass transport rates can also significantly affect the selectivity of Cu-based CO_2R.[8,9,13–18] Previous studies have shown that varying the size of copper nanoparticles between $20 - 70$ nm can increase C_2H_4 FE from <10% to ~40%[19], while the presence of Cu^+ species and

sub-surface oxygen has enhanced C_2H_4 FE to 60%.[20] Integrated solar fuels devices deployed outside must also contend with variability in incident solar irradiation and ambient temperature conditions, ranging from <0 – 50 °C, that will cause fluctuations in photovoltaic and electrochemical performance.[21] This further complicates product selectivity throughout the diurnal and annual cycles, with previous studies reporting that higher EC operating temperatures enhance overall total activity but increase H_2 selectivity at the cost of C_{2+} products.[13,22] Successfully translating bench-scale solar fuels experiments to the development of pilot-scale plants will require careful, intentional co-design of the electrocatalyst and photovoltaic to the environmental conditions of a specific deployment location. Recent work has begun to address this challenge, focusing on solar-driven hydrogen evolution[23–27] and solar-driven CO_2R under conditions of variable irradiation[28–33]. However, there remains a need to develop tools[34] that aid in understanding and predicting the transient, diurnal performance of integrated solar-fuels devices for complex, multi-product electrochemical reactions and the consequences of environmental conditions on the large-scale feasibility of these devices.

Herein, we develop a temperature and potential-dependent diurnal model that combines experimental results, consistent with previous electrochemical CO_2R reports[35–37], and real-world meteorological inputs (e.g., solar irradiance, ambient temperature) using computational regression, interpolation, and physics-based modeling techniques. This model is critical for bridging the gap between bench-scale experimental solar fuels devices and pilot-scale plants as it streamlines the location-specific co-design of the electrocatalytic and photovoltaic components of unassisted, integrated solar-driven CO_2R systems. A photovoltaic-electrochemical platform (PV-EC) was utilized as the foundation for the model, where the photovoltaic and electrochemical components are co-designed for operation, but where no semiconductor/liquid junction is present.[38] The model aims to streamline the experimental prototyping phase, by identifying electrolyzer configurations (e.g., from a selection of catalysts) that maximize generation of a target product, and to enable the effective, intentional co-design of CO_2R electrolyzers with large-scale PV modules. We analyzed the electrochemical CO_2R product formation of nine Cu-based electrocatalysts under standardized experimental conditions. To probe the effects of ambient temperature, the bulk electrolyte temperature was varied as a proxy. The experimental data was fed into a non-linear regression and interpolation model and coupled to a physics-based model to simulate the PV, which utilized real-world meteorological data, including solar irradiance, ambient temperature, and wind speed.[21] The combined model simulates the diurnal product output with a temporal resolution of 5 min, identifying changes in product output due to seasonal variations and environmental effects. Expanding upon these results, we modeled the scaled, annual output of ethylene, for a 1 MW solar farm[39,40], and the variations in annual product output which can be observed with changes in operating location. This work provides critical advancement in the implementation of solar-driven CO_2R devices by providing a tool to quantitatively predict the location-specific diurnal and annual product output from a large-scale PV-EC CO_2R system.

Results and Discussion

Methodology for predicting the diurnal and seasonal product output of PV-EC CO$_2$R devices

Figure 1 illustrates the methodology for the model, combining bench-scale experimental electrocatalysis measurements with meteorological data sourced from the NSRD to generate a predictive model for MW-scale, real-world device performance outputs (e.g., product generation, selectivity) as a function of the time of the day and time of the year. The model focuses on the diurnal gas-phase product output and selectivity of unassisted PV-EC CO$_2$R devices that use a Cu-based catalyst and do not require external electrical bias; however, the model is readily generalizable to any solar-driven electrochemical reaction. Using the model, we investigated the consequences of two significant environmental factors on the performance of unassisted PV-EC CO$_2$R devices: (1) varying incident solar irradiation and (2) varying temperature due to both device operation in ambient conditions and direct PV heating losses from irradiation.

A physics-based model, PVLIB[41], is employed to predict PV performance, with changes in incident irradiation and PV module temperature considered for all data shown. Key components of this model include input meteorological data from the NSRD[21], with a time resolution of 5 min, and the Faiman module temperature model[42] to capture the effects of ambient temperature, incident irradiation, convective heat transfer, and wind speed on the operating temperature of the PV module. To model the effect of incident solar irradiation on the operating point **(Figure S1)** and product distribution of the PV-EC CO$_2$R device, the model assumes that the initial experimentally observed electrochemical activity and selectivity is maintained throughout the diurnal cycle. We used a combination of interpolation and regression models, and iterative load-line analyses, to integrate the discrete experimental data with the continuous, modeled PV data. Further analyses for PV-EC CO$_2$R performance under conditions of assumed selectivity losses are also modeled **(see Note S1 for details)**.

In this manuscript, we characterized performance using the following metrics: Faradaic efficiency (FE, %) to refer to the selectivity of the gaseous CO$_2$R products, activity (J, mA cm^{-2}) to refer to the total current density observed on an electrocatalyst, productivity (J$_x$, mA cm^{-2}) to refer to the partial current density of specific products, and generation (tonne/yr) to refer to the annual generation of a specific PV-EC CO$_2$R product.
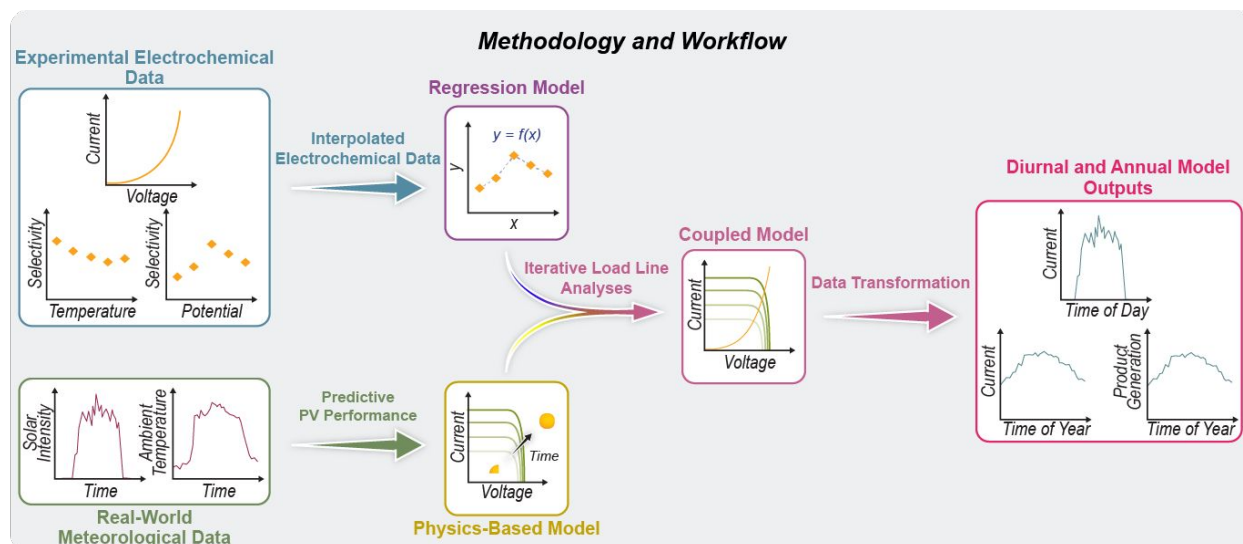
Figure 1. Flow diagram for the construction of the temperature and potential-dependent model. The model intakes experimentally derived electrocatalytic data describing the current-voltage characteristics, selectivity vs. voltage, and selectivity vs. temperature of the catalyst. This is combined with real-world meteorological data which the model transforms through the coupling of regression, interpolation, and physics-based modeling into outputs describing productivity vs. time of the day and product generation vs. time of the year.

Evaluating CO_2 reduction performance of Cu-based electrocatalysts

To collect the experimental electrochemical data required as the model input, we tested nine distinct Cu-based catalysts (**Table S1**) under standardized electrochemical conditions to establish a consistent baseline for comparison (**see Methods**). Multiple electrocatalysts were tested to develop one of the model's key features – the ability to identify the catalyst which maximizes the generation of a target product when coupled to a c-Si PV module with a maximum power output of 350 mW (**Figure S2**) under 1-sun intensity (1000 W m^{-2}). In this work, we targeted the production of ethylene, which is projected to reach a global market size of 287 billion USD by 2030[43] and has a CO_2 emissions footprint of 1.56 tonne CO_2/tonne ethylene[44]. Solar-driven CO_2R offers a pathway to decarbonizing the ethylene industry and to long-term storage of solar energy in molecular form.[45]

For Cu-based electrochemical CO_2R, numerous methods exist to steer selectivity and activity, including electrocatalytic methods such as catalyst morphology, loading, and chemical composition (e.g., oxides) and electrolyte-derived methods such as pH, flow rate, and electrolyte composition.[15–17,46–51] Each of these methods can be used to alter the electrochemical (EC) polarization curve, thereby changing the device operating point, which corresponds to the intersection between the EC polarization curve (current vs. voltage) and PV polarization curve (current vs. voltage) (**Figure S1**).[52] While it may be possible to dynamically vary electrolyte conditions to respond to diurnal variations, it is more difficult to alter the electrocatalyst, which is a fundamental driver of PV-EC CO_2R activity and selectivity. [8,9,21,53] Furthermore, it is costly

and time-consuming to optimize an electrocatalyst to a photovoltaic system using experimental methods only.[54–56]

We utilized a gas diffusion electrode (GDE) electrochemical flow cell (**Figure S3**) which has similar structure to the membrane electrode assemblies (MEA) commonly used to achieve industrially relevant current densities.[34,57,57,58] Using a non-zero gap GDE flow cell allowed for simple incorporation of a reference electrode to the electrochemical device, enabling ready measurement of cathode potential (E_{WE}), full cell voltage (V_{op}), and selectivity (FE). We investigated the effects of catalyst morphology, loading, and chemical composition, by employing three different fabrication methods (Cu sputtering, Cu_S; Cu e-beam deposition, Cu_e; Cu reactive oxide sputtering, CuO) with three relative loadings for each catalyst (LL = lowest loading, ML = medium loading, HL = high loading) (**Table S1, Figures S4 – S7**).

Figure 2 gives the Faradaic efficiency (FE) of the gaseous products (H_2, CO, C_2H_4, and CH_4) for each of the nine electrocatalysts vs. E_{WE} (**Figures S8 – 9**).[59–61] To connect the selectivity of the catalyst to the EC polarization curves, cyclic voltammetry was conducted prior to the potentiostatic experiments to determine the geometric current density (J_{geo}) vs. cell voltage (V_{op}) and J_{geo} vs E_{WE} behavior of each electrocatalyst (**Figure S10**). All nine of the catalysts exhibit similar trends in their H_2 and CO selectivity, with H_2 reaching a minimum from -0.69 to -0.79 V vs. RHE and CO decreasing with applied potential. The C_2H_4 maximum FE coincides with the H_2 minimum FE, reaching a value of ~35% for the $Cu_{s,HL}$ sample. At higher applied potentials, a deviation between catalysts occurs, with the CuO and lower loading Cu_S and Cu_e samples producing <10% FE for C_2H_4. As the C_2H_4 FE decreases, CH_4 FE rapidly increases, reaching ~40% CH_4 FE at -0.89 V vs. RHE, which aligns with observations from previous studies into Cu-based CO_2R.[9,51,62–64] While **Figure 2** gives a clear description of the electrocatalytic performance under the standardized conditions, it cannot alone predict the output when used in a PV-EC CO_2R under diurnal conditions.
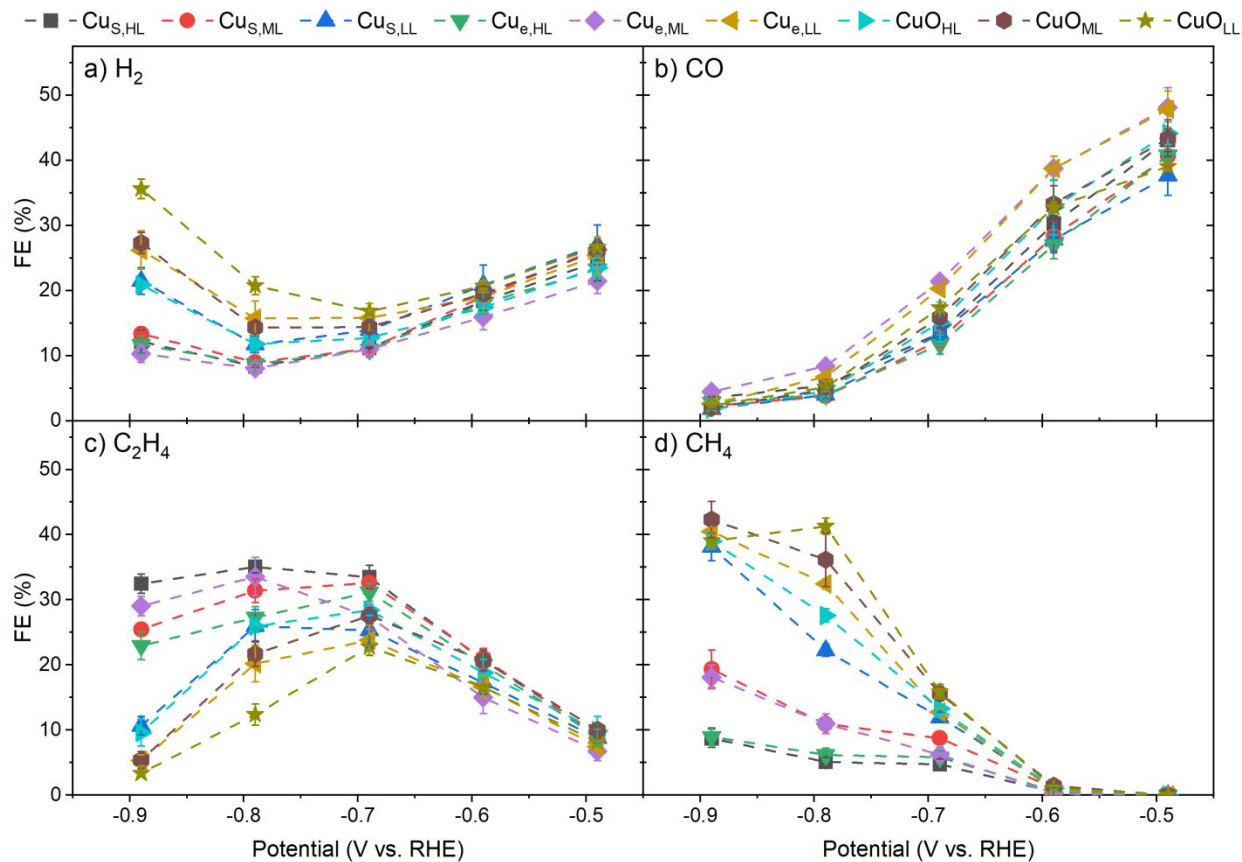
Figure 2. Faradaic efficiency of the gaseous products for (a) H_2, (b) CO, (c) C_2H_4, (d) CH_4 for CO_2R experiments conducted at various applied working electrode potentials (E_{WE} = -0.49, -0.59, -0.69, -0.79, -0.89 V vs. RHE) for each of the nine electrocatalysts. The selectivity was determined via gas chromatography sampled during potentiostatic measurements. The first subscript on the catalyst name (S, e) refers to the catalyst fabrication method (s = sputtering, e = electron-beam evaporation); CuO denotes catalysts fabricated via reactive oxide sputtering. The second subscript (LL, ML, HL) corresponds to the relative loading of the catalyst (LL = lowest loading, ML = medium loading, HL = highest loading). Error bars represent one standard deviation for at least three replicates.

Modeling the irradiance-driven diurnal output of PV-EC CO₂R devices

Using the electrochemical data from Figure 2, recorded at 22 ˚C, we first modeled the output of the PV-EC CO_2R devices under conditions of diurnal irradiance only, without the additional consideration of ambient temperature changes. **Figure 3** shows the results of the diurnal model for variations in incident irradiation, and compares the partial current density, J_x, of the four gas products over time, on the $Cu_{S,HL}$ electrocatalyst. This catalyst was selected as the representative due to the high ethylene outputs under conditions of diurnal irradiation variances only. The results of the model for each of the nine catalysts are available in **Table S2**.

7

Diurnal productivity for four representative days is given: the Winter solstice, Spring equinox, Summer solstice, and Fall equinox, using irradiation data for Barstow, CA in 2020.[21] Barstow was chosen for the model location as it has high average solar irradiation and currently houses large-scale concentrated solar and PV power generation.[65] **Figures S11 – 18** give the diurnal product output curves for the other eight electrocatalysts, while **Figure S19 – 27** shows the corresponding FE selectivity during these four days. In the early hours of the morning, and later hours of the evening, when incident irradiation is low, H_2 and CO are the dominant products. These hours correspond to points of low V_{op} and consequently, more positive E_{WE}, favoring the formation of CO (**Figure 2**).[8,9,66,67] During the middle of the day, when solar irradiation is highest, C_2H_4 productivity is maximized, with output greatest in the summer, when solar intensity is maximal. Despite the overall change in product selectivity throughout the day, the H_2:CO ratio is similar across the four seasons, maintaining a range between $0.6 – 0.8$. This range is consistent with the syngas ratio produced from coal gasification and presents an opportunity to utilize H_2 and CO generated from PV-EC CO_2R as a replacement feedstock for the Fischer-Tropsch process (**Figure S28**).[68,69] Additionally, the consistency in H_2:CO productivity ratio despite changes in total current density enables the future incorporation of unassisted integrated solar fuels CO_2R devices with downstream processes to further react these products.[70,71]

The 'choppy' data observed during the Spring equinox (**Figure 3b**) is attributed to variations in solar irradiation due to dynamic cloud coverage. Comparing the C_2H_4 output in the Spring equinox to the Fall equinox, a similar maximum J_{C2H4} is observed, with a maximum of $\sim$ -30 mA_{C2H4} cm^{-2} occurring around noon. However, the dynamic cloud coverage which is observed in the Spring equinox leads to significant fluctuations in the incident irradiation, and consequent operating point of the PV-EC device. This results in lower C_2H_4 produced throughout the Spring equinox, with a daily production (integral of productivity over 24 h converted to a mole basis, as described in eqn. (8)) of 0.42 ± 0.03 $mmol_{C2H4}$ cm^{-2} compared to 0.59 ± 0.04 $mmol_{C2H4}$ cm^{-2} during the Fall (**Table S3**). A similar trend is observed for the other three gaseous products. Dynamic cloud coverage is an important environmental factor to consider when choosing locations for siting PV-EC CO_2R devices as it can alter the device operating point over shorter timescales than those observed on sunny days. This sporadic change in operating point can reduce diurnal productivity and may have significant consequences for the reliability and durability of PV-EC CO_2R device output and its ability to be integrated to downstream processes. While the cloud coverage observed in this work corresponds only to the four specific days in 2020, it provides insight into the effect of meteorological changes on the operation of unassisted PV-EC CO_2R and should be investigated in future work to determine the long-term operation consequences of environmental phenomena on PV-EC CO_2R diurnal product output and stability.
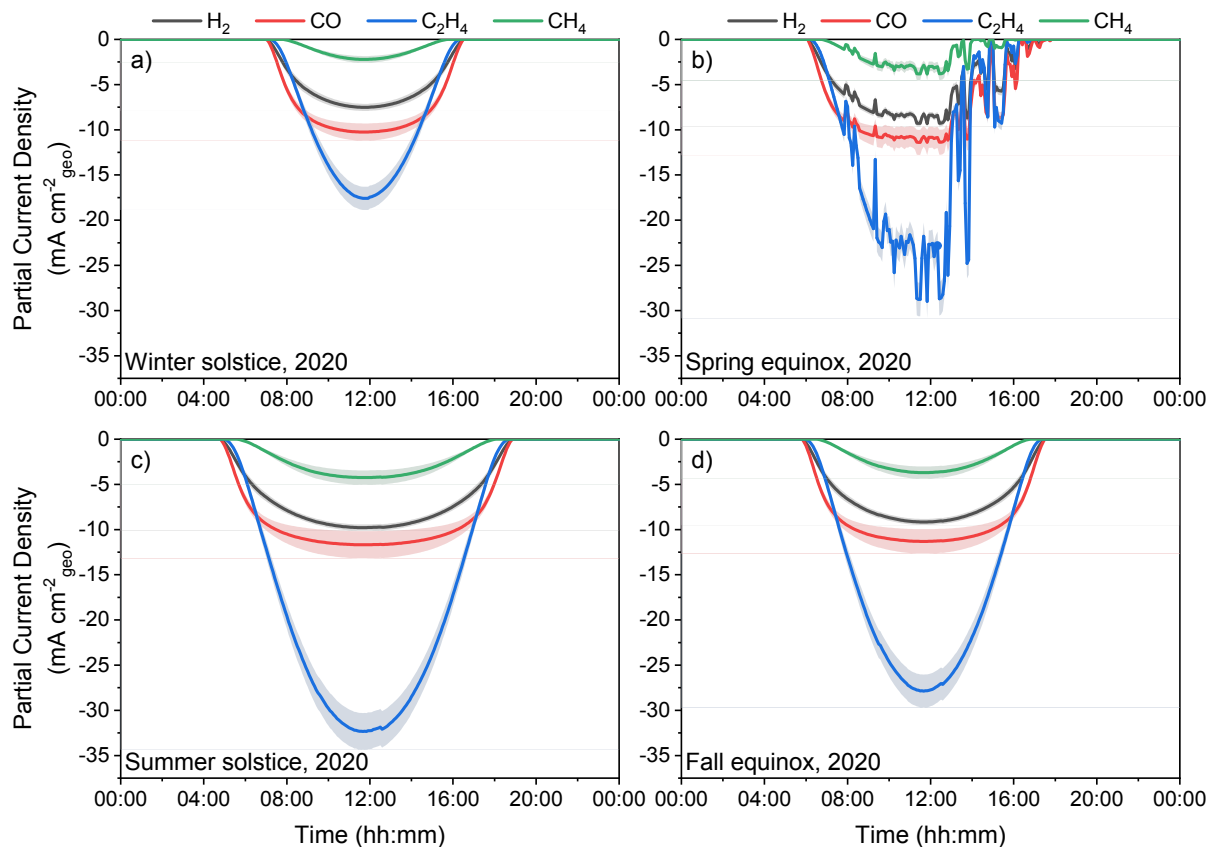
Figure 3. Modeling the diurnal product output of the $Cu_{S,HL}$ system for an Si PV, with a 1-sun maximum power output of 350 mW located at Barstow, CA, for four representative days throughout 2020. (a) Winter solstice, (b) Spring equinox, (c) Summer solstice, (d) Fall equinox. Shaded regions represent uncertainty to one standard deviation.

Modeling diurnal ambient temperature and irradiance effects in PV-EC CO_2R devices

To consider additional environmental effects on PV-EC CO_2R performance, we incorporated the effect of ambient temperature on electrochemical CO_2R performance into our coupled model. Previous studies have reported that temperature can significantly influence selectivity changes of CO_2R devices, with the extent of these effects varying with catalyst composition, electrolyte, and device configuration.[13,22,72] We utilized bulk electrolyte temperature as a proxy for ambient temperature and probed these effects using the $Cu_{s,HL}$ catalyst at temperatures of 5 ˚C, 15 ˚C, 22 ˚C, 35 ˚C, and 48.5 ˚C ± 0.5 ˚C (**see Note S1**). Electrochemical experiments were conducted in a similar process to the irradiance analysis, with cyclic voltammetry to produce EC polarization curves (J_{geo} vs. V_{op} and J_{geo} vs. E_{WE}) (**Figure S29**) followed by chronoamperometry to determine the selectivity (FE) for the gaseous products (**Figure S30**).

Increasing bulk electrolyte temperature, and consequently the temperature at the reaction interface, results in increased reaction rates and electrolyte conductivity.[13,73,74] In the EC polarization curves, these results manifest as increases in total current density and more positive E_{WE} values at higher temperatures for a given V_{op} (**Figure S29**). Each product exhibits a different temperature

9

dependence, with increasing temperatures resulting in greater selectivity towards H_2, decreases in the selectivity of C_2H_4 and CH_4, and negligible change in CO selectivity. In addition to changes in reaction kinetics, these trends with temperature are also likely a function of factors including decreases in CO_2 solubility with increasing temperature, changes in the buffer reactions of the CO_2-bicarbonate system, changes in transport properties, and products with higher activation energy (e.g., C_2H_4 and CH_4) being more sensitive to increases in the operating temperature.[75]

The model integrates the influence of temperature by identifying the ambient temperature associated with the specific time of day and subsequently executing a load-line analysis to identify the operating point as a function of the PV polarization curve and relevant temperature-dependent EC polarization curve (Figure 1b).[76] This process is repeated to generate an array of operating points throughout the day as a function of both irradiance and ambient temperature. **Figure 4** describes the output of this process, comparing the partial current density of C_2H_4, CH_4, CO, and H_2 during the Summer solstice, on the $Cu_{S,HL}$ catalyst, under 'variable irradiance only' and 'variable irradiance and ambient temperature' conditions. During the Summer solstice, the ambient temperatures reach a maximum of 38.5 °C (**Figure S31**) which enhances H_2 and CO productivity. C_2H_4 productivity is negligibly affected while CH_4 productivity decreases by over two-fold. An analysis of the syngas ratio across all the seasons results in a wider range of H_2:CO ratios observed, from $0.6 - 1.0$ (**Figures S32 – 34**). The syngas ratio is most significantly affected by ambient temperature during the winter, where the colder temperatures favor C_2H_4 selectivity at the cost of H_2 selectivity, and in the spring, where dynamic cloud coverage appears to increase the syngas ratio. While this larger ratio range will require more care with downstream reactors, the observed ratios are still within the boundaries of those obtained by conventional coal gasification (**Figure S35**).[68,69]

In the summer, spring, and fall, negligible changes in C_2H_4 productivity are observed, indicating that the decreases in selectivity observed with warmer temperatures are balanced by the increase in total activity (**Table S4**). Comparatively, in the winter, a 25% increase in C_2H_4 productivity occurs, suggesting that C_2H_4 productivity could be optimized in warmer months through device cooling methods which increase C_2H_4 selectivity while maintaining moderate total activity. A similar phenomenon occurs for CH_4, highlighting that device cooling mechanisms could be a powerful technique for steering diurnal product outputs. Ambient temperature also affects the shape of the diurnal productivity curves, skewing the H_2 and CO maximum productivity to the right, after the irradiance maximum. This is likely due to a delayed increase in ambient temperature which increases total activity. For C_2H_4 and CH_4, two peaks are observed, occurring before and after the maximum irradiance and further emphasizing the balance between temperature and selectivity which must be maintained to maximize the productivity of temperature sensitive products.
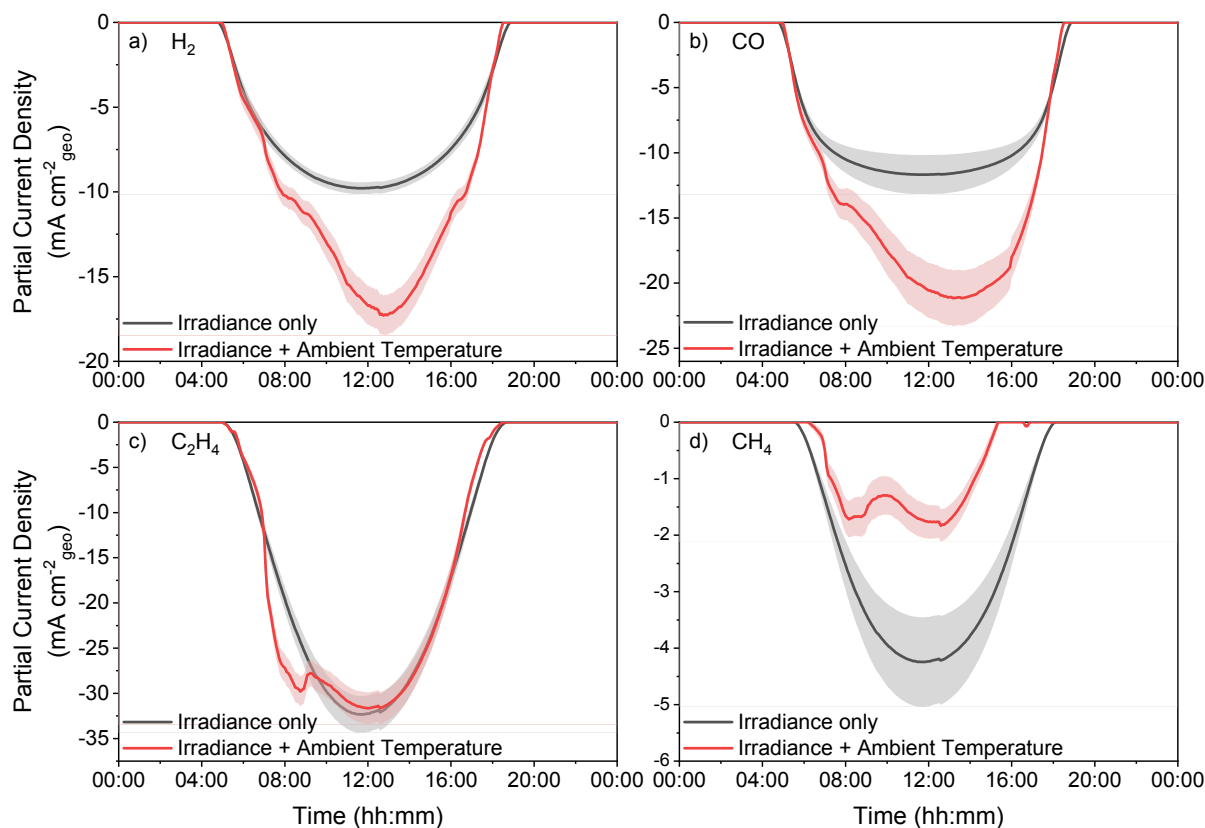
Figure 4. Comparison of the diurnal output of the $Cu_{S,HL}$ system during the Summer solstice, when only irradiance is considered vs. when irradiance and ambient temperature are considered. Data shown corresponds to the gaseous products, (A) H_2, (B) CO, (C) C_2H_4, and (D) CH_4. Error bars represent one standard deviation. Corresponding figures for the $Cu_{S,HL}$ system for the winter solstice, spring equinox, and fall equinox are given in **Figures S32 – 34.**

The effects of scale and location on annual ethylene generation

Expanding upon the diurnal product output model, we calculated the average annual ethylene generation for a hypothetical 1 MW solar farm, by calculating a scaling factor based on the maximum power output of the modeled Si PV under 1-sun intensity, 350 mW **(Note S2, Figure S36)**. The resulting output from Barstow, CA was compared to those of PV-EC CO_2R devices located in Beijing, CN and Sydney, AUS. The calculation assumes that the scaled electrochemical device ($\sim$300 m^2, divided into different electrochemical cells) maintains the selectivity and activity observed for the 1 cm^2 device. In practice, this performance is likely to have significant differences, and would involve utilizing an MEA over a GDE flow cell; however, this work aims to demonstrate the utility of the model and to highlight the impact of meteorological factors and location on product output. As data from scaled-up electrochemical cells (e.g., 1 m^2 MEA) becomes available, it can be readily incorporated into our existing model to determine scaled PV-EC CO_2R performance.

11

Figure 5 provides a comparison of the scaled, annual results for the three locations. These results correspond to an ideal PV-EC CO_2R device in which no catalyst performance degradation occurs. Under these conditions, Barstow produces the most ethylene via unassisted PV-EC CO_2R, generating 18.5 tonne/yr compared to 12.3 tonne /yr for Beijing and 13.7 tonne/yr for Sydney (**Table S5**). The annual output curve for Barstow also varies less than the other two locations, emphasizing the effect of dynamic cloud coverage and weather events on the output of PV-EC CO_2R devices. A particular factor experienced in Beijing is temperatures which fall outside of the experimental operating range (0 – 48.5 °C) during hours of irradiation. At temperatures outside of this range, it is no longer optimal to operate device, as this could risk damaging the electrochemical components; below 0 °C, issues of electrolyte freezing and mass transport arise, while above 50 °C, we observed deformation of the anion exchange membrane.[77,78] At these temperature extremes, the model assumes that the PV-EC device will not be operated to protect the device equipment (e.g., wind turbine cut-out speed).[79] However, future work could model the use of heating or cooling mechanisms to control the temperature of the device in the extreme temperature regions and begin to consider greater degrees of engineering complexity to assess the viability of operating solar-driven devices during nighttime or periods of excess electricity generation from the grid.

The development of stable CO_2R electrocatalysts is ongoing, with state-of-the-art catalysts reaching operational lifetimes over 100 hours; however, most Cu-based catalysts exhibit stability on the scale of tens of hours.[80–83] Therefore, we conducted a preliminary analysis to begin considering the impact of catalyst degradation on product output and operating lifetimes (**Figures S37 − 38**). We modeled the annual generation curves for Barstow, CA, incorporating constant ethylene activity loss over 24 h periods (e.g., % decrease in C_2H_4 partial current density from initial) and specifying minimum performance thresholds of ethylene activity (e.g., 60/80% of original partial current density) for the catalyst before it would be replaced. These results indicate that the minimum performance threshold has a stronger influence on annual generation than to the rate of activity loss. A 10% loss in annual C_2H_4 generation (1.9 tonne C_2H_4/yr) compared to the ideal scenario is observed for a minimum threshold of 80% relative activity while a 20% loss (3.7 tonne C_2H_4/yr) occurs for a minimum threshold of 60% relative activity. Changing the degradation rate with a constant minimum threshold negligibly affected the annual output; however, the cost of changing the catalyst more frequently is expected to increase the cost of the output product.

The diurnal and annual model we have developed provides a tool to streamline the scaling of solar-driven electrochemical technologies from bench-scale experimental results to larger installations. This model offers a bridge between bench-scale experiments and pilot scale operation by identifying, from various electrocatalyst and photovoltaic configurations, the configuration which optimizes the generation of a target product under varying meteorological conditions and solar irradiances at a specific location. Continued efforts to build upon this diurnal and annual model can accelerate the deployment of scaled solar-driven CO_2R pilot plants, which will be required to construct fully validated models of large-scale systems that wholly capture the transient influences of location-specific irradiance, temperature, and other environmental factors. Previous research into semi-empirical regression modeling for scaled alkaline[84] and PEM water electrolyzers[85,86], and electrochemical CO_2 reduction[34,87], has highlighted the need for the synergistic pairing of modeling and experimental results to inform each progressive point of scaling.

While this work presents a first step to enabling efficient, economic scaling of solar-driven electrochemical technologies, it has also identified areas of future work which should be considered. Key areas include: (1) understanding long-term durability of electrocatalysts, under steady and variable operating conditions; and (2) identifying unique challenges which arise when electrode and photovoltaic areas are scaled to the sizes required to operate a 1 MW+ scale solar fuels plant. As research and development efforts in this area progress, the model can be adapted to account for long-term degradation and challenges with device scaling. With progressions in scaling, it will be important to consider the integration of electrochemical solar fuels devices into the broader chemicals manufacturing infrastructure. In this vein, some important areas to research will include: (1) the integration of solar-driven electrochemical devices with upstream (e.g., potentially impure CO_2 streams) and downstream processes (e.g., syngas in existing thermochemical infrastructures) and the effects of variable outlet stream ratios on these processes; (2) detailed technoeconomic analyses (TEAs), life-cycle assessments (LCAs), studies of energy return on energy invested (EROEI), and environmental impact studies, among others, to obtain more accurate predictions of the environmental, climate, socio-economic, and sustainability benefits of solar fuels technologies; (3) the consequences of different electrochemical cell architectures and chemistries (e.g., alternative anode chemistries) on the diurnal and yearly output of solar fuels devices; and (4) develop a deeper understanding of the benefits of operating cell configurations under conditions of diurnal and stored electrical (or chemical) power to determine the role of solar-driven electrochemical technologies in the broader discussion of energy storage and grid balancing.
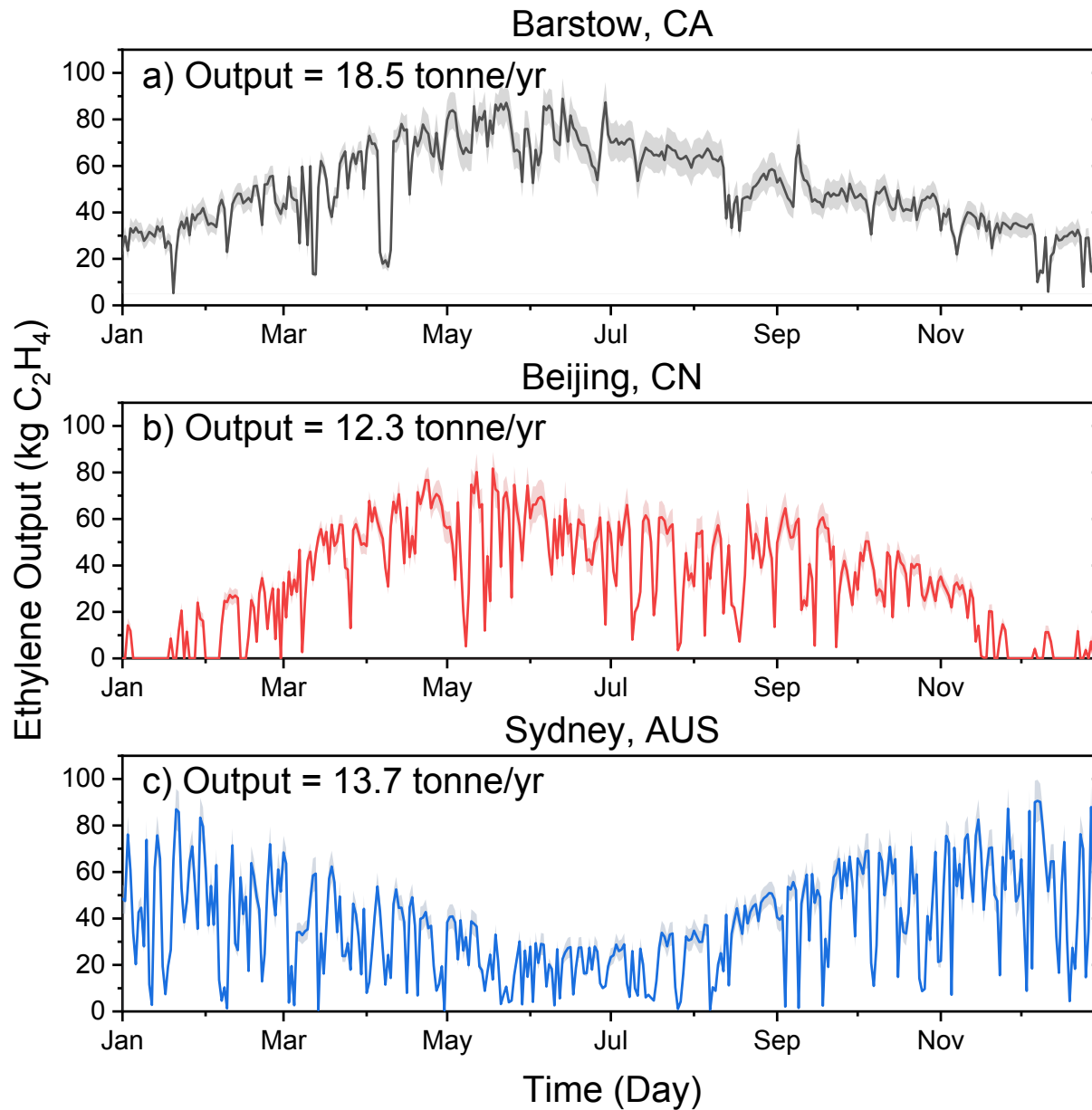
Figure 5. Annual output of $Cu_{S,HL}$ PV-EC CO_2R device for a PV-EC CO_2R device scaled to a 1 MW solar farm located in: (a) Barstow, CA; (b) Beijing, CN; (c) Sydney, AUS. Shaded regions represent error to one standard deviation.

Conclusion

We have developed a temperature and potential-dependent model capable of converting bench-scale electrochemical results into quantifiable product outputs under dynamic diurnal operating conditions (i.e., diurnal product output curves). Using electrochemical characterization (e.g., cyclic voltammograms, FE) in combination with real-world meteorological data, we investigated the consequences of meteorological and environmental effects on the performance of an unassisted PV-EC CO_2R device. We investigated the CO_2R performance of nine Cu-based catalysts across standardized experimental conditions and combined these results with a physics-based model of a Si PV module. In addition to capturing the effects of diurnal irradiance on productivity, with CO and H_2 productivity dominant in the early and late hours of the day, and C_2H_4 productivity dominant during the middle of the day, the model captures environmental effects such as dynamic cloud coverage and provides insight into their resultant consequences on target product activity. Utilizing bulk electrolyte temperature as a proxy for ambient temperature, we observed that enhanced temperatures increase H_2 and CO activity, but that the H_2:CO outlet ratio remains comparable to syngas derived from coal gasification and could be used for downstream reaction processes. Additionally, we found that C_2H_4 and CH_4 are particularly sensitive to warmer temperatures and propose that device cooling mechanisms could be key to maximizing C_2H_4 output in warmer seasons (e.g., summer, fall) and in locations that experience extreme heat waves. Finally, we developed an annual model of product output, scaled to a 1 MW solar farm, to probe the consequences of siting location and catalyst degradation on annual ethylene generation. We observed a maximum generation of 18.5 tonne C_2H_4/yr at Barstow, CA and note that while integrated solar fuels devices have flexibility in their location, local climates could significantly affect their performance. The future deployment of solar-driven CO_2R devices will require a synergistic pairing of modeling and experimental results, with these models and results being updated cyclically as progress toward scale-up informs next-generation designs. By integrating computation with experimental data, this work has developed a first step towards scaling of solar-driven CO_2R devices and can be used to optimize the location-specific output of a target electrochemical product for integration of solar fuels technology into broader chemicals manufacturing processes.

<u>Methods</u>

Copper Electrocatalyst Deposition Methods

Sigracet 39 BB (Fuel Cell Store) carbon paper was cut into 6 x 6 cm^2 pieces. The Cu electrocatalyst was deposited on the PTFE-treated side of the microporous layer. For the e-beam deposited samples, an AJA e-beam evaporator was used to deposit either 50 nm, 100 nm, or 200 nm of Cu at a rate of 1 Å/s. For the sputtered samples, Cu was sputtered at three different power settings: 200 W, 100 W, and 50 W for 600 s using a Lesker sputterer. For the CuO samples, reactive oxide sputtering was conducted on the Lesker sputterer by flowing O_2 at a flow rate of 4 sccm, with Ar flowing at 20 sccm. Following deposition of the catalyst layer, the electrode was cut into 1.5 x 1.5 cm^2. Electrical connection was made to the catalyst via Cu electrical tape.

Electrocatalyst Characterization

X-ray photoelectron spectroscopy (XPS) was used to analyze the surface of the electrodes pre- and post- electrolysis. Survey and high-resolution spectra were obtained using a PHI VersaProbe 3 XPS instrument with monochromatized Al Kα (1486.4 eV) radiation in the Stanford Nano Shared Facilities. Survey spectra were conducted on a 200 μm spot size to identify specific binding energies of interest using a pass energy of 224 eV with a 0.8 eV step size. High-resolution spectra were conducted on the same spot using a 55 eV pass energy with a 0.1 eV step size to identify surface chemical composition and oxidation states. An ion gun (2kV, 1.5μA) was used to sputter through the oxidized surfaces for 3 min after the initial survey and high-resolution spectra were collected. Automatic charge neutralization was used during sputtering to prevent charging effects and a total of ~15 - 20 nm was removed using SiO_2 on Si wafer as a reference. Survey and high-resolution spectra were collected again on the sputtered surfaces. The spectra were calibrated to the adventitious C 1s peak at 284.8 eV. Peak fitting was performed using Shirley backgrounds and Gaussian-Lorentzian line shapes in CasaXPS software.

Scanning electron microscopy (SEM) was conducted using an FEI Magellan 400 XHR Scanning Electron Microscope to determine the morphology of the catalyst surface. An electron beam of 2 kV and 25 pA was used, and the samples were supported by conductive silver paint.

Electrochemical Cell Setup

A gas diffusion electrochemical flow cell was constructed according to **Figure S3** with an active working electrode geometric area of 1 cm^2 and a counter electrode area of 4.0 cm^2. The counter electrode was oversized to reduce the overpotential required to drive the oxygen evolution reaction. The porous Cu electrodes were used as the cathode, with Ni foil as the counter electrode, and an Ag/AgCl reference electrode in the cathode chamber. The catholyte and anolyte reservoirs each contained 13 mL of 1.0 M potassium hydroxide (KOH, Sigma-Aldrich, semiconductor grade, 99.99% trace metals basis) which was circulated through the electrochemical cell at 2 mL/min. A Sustainion anion exchange membrane (Dioxide Materials) was used to separate the working and counter electrode compartments to prevent product crossover. Electrochemistry was performed using a Biologic VMP3 potentiostat. Cyclic voltammetry (CV) measurements were performed to determine the full cell and working electrode polarization curves for a particular sample. For the

CV measurements, potentiostatic electrochemical impedance spectroscopy (PEIS) measurements were conducted after the experiment (to ensure that the full cell polarization curve reported completely uncompensated potentials between 1.5 and 4 V), and the measured resistance was compensated by 85% to prevent overcompensation over the large current range tested. Chronoamperometry was conducted at five potentials in 15 min intervals (-0.49, -0.59, -0.69, -0.79, and -0.89 V vs. RHE), for a total of 1 h 15 min, with PEIS and ZIR used to compensate for 85% of the measured resistance before the potential hold.

CO_2 Reduction Product Analysis

For all potential holds, gases were sampled every 15 min, once for each potential, by a gas chromatograph (GC) (SRI Instruments, MG#5). The GC was equipped with a flame ionization detector (FID) to measure carbonaceous gas products and a thermal conductivity detector (TCD) to measure H_2 gas. The signal response of the FID and TCD was calibrated by comparison to a series of NIST-traceable standard gas mixtures (Airgas Inc.). The catholyte was analyzed after electrolysis via ^1H NMR using a Varian Inova 600 MHz NMR machine with phenol and DMSO internal standards. These results were quantified by comparison to an external standard calibration curve of the CO_2 reduction products.

Temperature Setup

An Isotemp 3016S Recirculating Chiller was used to achieve bulk electrolyte temperatures of 5°C, 15°C, 35°C, and 48.5°C, with a ±0.5°C error, in the electrochemical cell. The cell was placed approximately 10 mm above the water bath. The electrolyte reservoirs and the tubing connecting them to the cell were submerged in the water bath. The volume of the reservoirs and the length of the tubing were also adjusted to achieve the target temperatures in the cell. The reservoir volumes for the 5°C, 15°C, 35°C, and 48.5°C temperatures were 20mL, 15mL, 20mL, and 30mL respectively.

To determine the chiller settings required to achieve the desired temperatures, an AMPROBE Multilogger thermometer was inserted into the cell to measure the temperature of the bulk electrolyte. For these experiments, MilliQ water was used as the electrolyte to prevent the corrosion of the thermocouple inserted into the cell. The temperature of the cell was monitored for at least 60 min, to determine how long it would take for the system's temperature to fully equilibrate (i.e., no temperature change within the cell for > 20 min). The chiller operating temperatures for the 5°C, 15°C, 35°C, and 48.5°C temperatures were 3.5°C, 14.2°C, 38.7°C, and 58.0°C respectively. For 5°C and 15°C, 15 min of waiting time was necessary for the temperature in the cell to equilibrate, while for 35°C and 48.5°C 30 min was necessary. For the electrochemical experiments at various operating temperatures, the original electrochemical cell setup was utilized, with 1 M KOH in the electrolyte reservoirs.

Silicon Photovoltaic Model

To simulate the multi-cell silicon photovoltaic (PV) module, a combination of literature-defined and calculated PV parameters for a single c-Si diode ($V_g = 1.12\ eV$) solar cell at the Shockley-

Queisser radiative efficiency limit (S-Q limit) under AM 1.5G solar illumination were used.[88,89] The current-voltage (I-V) polarization curve for a single-diode equation was defined as:

$$i = i_{sc} - i_o \left[\exp\left(\frac{qV}{nkT}\right) - 1 \right], \tag{1}$$

where i_{sc}, i_o, and V are the short-circuit current, dark-saturation current, and cell potential, respectively. Moreover, q, n, k, and T are the fundamental charge of an electron, diode ideality factor, Boltzmann's constant, and temperature of the solar cell respectively. It is important to note that for silicon solar cells simulated at the S-Q limit, the short-circuit current and open circuit voltage V_{oc} play the most deterministic roles in the overall shape of the I-V curve.

Integrating over the solar spectral irradiance ($I(\lambda)$), with respect to wavelength, the short-circuit current density for a single diode c-Si ($V_g = 1.12\ eV$) solar cell was defined[90]:

$$j_{sc} = \frac{i_{sc}}{A} = \frac{q}{hc} X \int_0^{\frac{hc}{qV_g}} I(\lambda) \lambda d\lambda, \tag{2}$$

where h, c, X, V_g, A, and λ are Planck's constant, speed of light, solar concentration, the semiconductor bandgap, solar cell area, and photon wavelength, respectively. The solar concentration is calculated with the following,

$$X = \frac{I}{I_{AM1.5G}}, \tag{3}$$

where I is the solar irradiance from NREL's TMY3 datasets and $I_{AM1.5G}$ is the total solar irradiance at AM 1.5G conditions (100 mW cm^{-2}).

Rearranging eqn. 1 for open-circuit conditions ($V = V_{oc}$, $i = 0$) and expressing currents as current densities (normalized by the same solar cell area A), the dark-saturation current density was calculated as follows:

$$j_o = \frac{i_o}{A} = \frac{j_{sc}}{\exp\left(\frac{qV_{oc}}{nkT}\right) - 1}. \tag{4}$$

Using j_{sc} calculated under full illumination ($X = 1$) AM 1.5G conditions specified by NREL (43.7 mA cm^{-2}) and the V_{oc} for standard c-Si solar cells (~680 mV[91]), j_o was determined to be 1.49×10^{-10} mA cm^{-2}. To achieve a 100 mA short-circuit current, solar cells of $A = 2.29\ cm^2$ are needed and was subsequently multiplied by j_{sc} and j_o to recover the total short-circuit current and dark-saturation current. A Si PV module based on this single-diode solar cell would require approximately 6 PV cells in series ($N_s = 6$) to achieve the required V_{oc} (4.1 V) to generate appreciable FE to ethylene.

The temperature of the solar cell module throughout the day as it is heated by the sun and convectively cooled by the wind was estimated using the Faiman module temperature model[42]:

$$T = T_a + E_{POA} \frac{\alpha(1 - \eta_m)}{U_0 + U_1 \times WS}, \tag{5}$$

18

where T_a, α, E_{POA}, η_m, U_0, U_1, WS are the ambient air temperature, absorption coefficient of the module, irradiance incident on the plane of the module, efficiency of the PV module, convective heat transfer coefficient intercept, convective heat transfer coefficient slope, and wind speed respectively. The ambient air temperatures, windspeeds, and solar irradiances are obtained from 2020 NREL TMY3 dataset for Barstow, CA throughout the diurnal (datapoints every 5 min) and annual cycles (data points every 60 min).[21]

Assuming the multi-cell PV module has zero series resistance and negligibly large shunt resistance, these main parameters (solar irradiance I, temperature of the solar cell T, i_{sc}, and i_o) were fed into the MATLAB coding package, PVLIB, an open-source toolbox developed by Sandia National Laboratories. The package uses PVsyst to recalculate i_{sc} and i_o as a function of solar irradiance and temperature of the solar cell, allowing for the construction of PV I-V curves (according to eqn. 1) with time series data specified throughout the day and year.[41] Additional parameters used to simulate the PV module are listed in **Table 1**.

Table 1: Parameters for modeling the PV module comprised of multiple c-Si solar cells.

Parameter	Value	Units	Reference
n	1	-	88
μ_n	-0.0003	K^{-1}	41
$\alpha_{sh,exp}$	5.5	$m^2\,s^{-1}$	41
$\alpha_{i_{sc}}$	-0.002	$A\,K^{-1}$	41
α_{abs}	1	-	88
η	0.33	-	92
U_0	25	$W\,m^{-2}\,K^{-1}$	42
U_1	6.84	$W\,m^{-3}\,s\,K^{-1}$	42

Diurnal Model

To model the diurnal output of the electrochemical cell, constrained by the I-V behavior of the PV module, a smoothing spline regression function ($p = 0.99$) was fitted to the experimental electrochemical polarization curve (total current i_{tot} vs. device operating potential V_{op}). Because the active working electrode geometric area was 1 cm^2, the use of current and current density in this analysis is synonymous. The cathode potential, E_{we}, was also related to V_{op} with a smoothing spline regression ($p = 0.9999$).

19

To perform a similar analysis on the partial current densities j_i, the discrete experimental j_i was calculated as the product between i_{tot} from the cyclic voltammetry experiment and the FEs from the chronoamperometry experiments, both matched to the same E_{we},

$$j_i = i_{tot,CV}(E_{we}) \times \frac{FE_{i,CA}(E_{we})}{100}.$$

(6)

The discrete j_i was then fitted to a smoothing spline regression (p = 0.995) as a function of E_{we}. Therefore, if a V_{op} was identified, it was mapped to a corresponding i_{tot} and E_{we}, which was then further converted to j_i. FE was determined by dividing the calculated j_i by the same i_{tot} identified at V_{op} and E_{we}. Because FEs were only measured at a select few E_{we}, the error in experimental FE at all E_{we} was reasonably assumed from a modified Akima piecewise cubic Hermite interpolation function. The error in j_i was calculated with standard error propagation methods as follows:

$$\delta j_i = j_i \left[\left(\frac{\delta i_{tot}}{i_{tot}} \right)^2 + \left(\frac{\delta FE_i}{FE_i} \right)^2 \right]^{\frac{1}{2}}.$$

(7)

Inputting the solar irradiance, ambient air temperature, and windspeed into PVLIB, the I-V curves from the PV module throughout the day are calculated. V_{op} for each PV I-V curve is calculated by finding the intersection between the PV I-V curves and the experimentally measured electrochemical polarization curves using MATLAB's fsolve() function. This point is then related to the product FE and j_i by calculating the expected E_{we} using V_{op}, with the assumption of an ideal electrochemical CO_2R system such that at constant E_{we}, FE remains constant. j_i was then used to model the total product output throughout the diurnal cycle. The same overall approach is utilized to analyze the device's performance over an annual timescale.

To determine the specific molar production throughout the year, the specific partial current, i_i, is integrated with respect to time to obtain the expected charge passed to that product in the device. Faraday's law of electrolysis is used to convert electrical charge, Q, into moles of product, n_{mol},

$$n_{mol} = \frac{Q}{vF},$$

(8)

where v is the number of electrons involved in the specific half reaction.

Temperature Model

A similar approach is used to incorporate ambient temperature into the PV-EC simulations, except that an additional degree of freedom must now be considered in the 3D regression functions. Locally weighted smoothing linear regression (lowess) functions with spans = 0.4 and 0.2 were used to express i_{tot} as a function of V_{op} and temperature and V_{op} as a function of E_{we} and temperature respectively. Additionally, lowess regressions with spans = 0.2 were used to describe j_i as a function of E_{we} and temperature. Biharmonic spline interpolation (MATLAB® 4 griddata method) was used to model the error found between experimentally collected data points (interpolation between temperatures and E_{we}). The error in j_i is propagated according to eqn. 7.

Author Contributions

K.M.K.Y. and W.J.W. contributed equally to the ideation of the project, development of the model, and writing of the manuscript. M. R. P., L. W., S.L. contributed to the completion of experimental results and characterization. A.J.K. and J.C.B. contributed to the development of the model and writing of the manuscript. A.Z.W., A.T.B., A.C.N., and T.F.J. aided in the development of the project and writing of the manuscript.

Conflicts of Interest

The authors declare no conflicts of interest.

Acknowledgements

References

(1) Khoo, H. H.; Halim, I.; Handoko, A. D. LCA of Electrochemical Reduction of CO2 to Ethylene. *J. CO2 Util.* **2020**, *41*, 101229. https://doi.org/10.1016/j.jcou.2020.101229.

(2) Leonzio, G.; Chachuat, B.; Shah, N. Towards Ethylene Production from Carbon Dioxide: Economic and Global Warming Potential Assessment. *Sustain. Prod. Consum.* **2023**, *43*, 124–139. https://doi.org/10.1016/j.spc.2023.10.015.

(3) Kato, N.; Mizuno, S.; Shiozawa, M.; Nojiri, N.; Kawai, Y.; Fukumoto, K.; Morikawa, T.; Takeda, Y. A Large-Sized Cell for Solar-Driven CO2 Conversion with a Solar-to-Formate Conversion Efficiency of 7.2%. *Joule* **2021**, *5* (3), 687–705. https://doi.org/10.1016/j.joule.2021.01.002.

(4) Basic Energy Sciences Roundtable. *Report of the Basic Energy Sciences Roundtable on Liquid Solar Fuels*; 2019. https://doi.org/10.2172/1615599.

(5) Creissen, C. E.; Fontecave, M. Solar-Driven Electrochemical CO2 Reduction with Heterogeneous Catalysts. *Adv. Energy Mater.* **2021**, *11* (43), 2002652. https://doi.org/10.1002/aenm.202002652.

(6) Ardo, S.; Rivas, D. F.; Modestino, M. A.; Greiving, V. S.; Abdi, F. F.; Llado, E. A.; Artero, V.; Ayers, K.; Battaglia, C.; Becker, J.-P.; Bederak, D.; Berger, A.; Buda, F.; Chinello, E.; Dam, B.; Palma, V. D.; Edvinsson, T.; Fujii, K.; Gardeniers, H.; Geerlings, H.; Hashemi, S. M. H.; Haussener, S.; Houle, F.; Huskens, J.; James, B. D.; Konrad, K.; Kudo, A.; Kunturu, P. P.; Lohse, D.; Mei, B.; Miller, E. L.; Moore, G. F.; Muller, J.; Orchard, K. L.; Rosser, T. E.; Saadi, F. H.; Schüttauf, J.-W.; Seger, B.; Sheehan, S. W.; Smith, W. A.; Spurgeon, J.; Tang, M. H.; Krol, R. van de; Vesborg, P. C. K.; Westerik, P. Pathways to Electrochemical Solar-Hydrogen Technologies. *Energy Environ. Sci.* **2018**, *11* (10), 2768–2783. https://doi.org/10.1039/C7EE03639F.

(7) Montoya, J. H.; Seitz, L. C.; Chakthranont, P.; Vojvodic, A.; Jaramillo, T. F.; Nørskov, J. K. Materials for Solar Fuels and Chemicals. *Nat. Mater.* **2017**, *16* (1), 70–81. https://doi.org/10.1038/nmat4778.

(8) Kuhl, K. P.; Cave, E. R.; Abram, D. N.; Jaramillo, T. F. New Insights into the Electrochemical Reduction of Carbon Dioxide on Metallic Copper Surfaces. *Energy Environ. Sci.* **2012**, *5* (5), 7050–7059. https://doi.org/10.1039/C2EE21234J.

(9) Nitopi, S.; Bertheussen, E.; Scott, S. B.; Liu, X.; Engstfeld, A. K.; Horch, S.; Seger, B.; Stephens, I. E. L.; Chan, K.; Hahn, C.; Nørskov, J. K.; Jaramillo, T. F.; Chorkendorff, I. Progress and Perspectives of Electrochemical CO₂ Reduction on Copper in Aqueous Electrolyte. *Chem. Rev.* **2019**, *119* (12), 7610–7672. https://doi.org/10.1021/acs.chemrev.8b00705.

(10) Thevenon, A.; Rosas-Hernández, A.; Peters, J. C.; Agapie, T. In-Situ Nanostructuring and Stabilization of Polycrystalline Copper by an Organic Salt Additive Promotes Electrocatalytic CO2 Reduction to Ethylene. *Angew. Chem.* **2019**, *131* (47), 17108–17114. https://doi.org/10.1002/ange.201907935.

(11) Zhang, Z.; Bian, L.; Tian, H.; Liu, Y.; Bando, Y.; Yamauchi, Y.; Wang, Z.-L. Tailoring the Surface and Interface Structures of Copper-Based Catalysts for Electrochemical Reduction of CO2 to Ethylene and Ethanol. *Small* **2022**, *18* (18), 2107450. https://doi.org/10.1002/smll.202107450.

(12) Huang, Y.; Handoko, A. D.; Hirunsit, P.; Yeo, B. S. Electrochemical Reduction of CO2 Using Copper Single-Crystal Surfaces: Effects of CO* Coverage on the Selective Formation of Ethylene. *ACS Catal.* **2017**, *7* (3), 1749–1756. https://doi.org/10.1021/acscatal.6b03147.

(13) Vos, R. E.; Kolmeijer, K. E.; Jacobs, T. S.; van der Stam, W.; Weckhuysen, B. M.; Koper, M. T. M. How Temperature Affects the Selectivity of the Electrochemical CO2 Reduction on Copper. *ACS Catal.* **2023**, *13* (12), 8080–8091. https://doi.org/10.1021/acscatal.3c00706.

(14) Rossi, K.; Buonsanti, R. Shaping Copper Nanocatalysts to Steer Selectivity in the Electrochemical CO2 Reduction Reaction. *Acc. Chem. Res.* **2022**, *55* (5), 629–637. https://doi.org/10.1021/acs.accounts.1c00673.

(15) Zhang, G.; Zhao, Z.-J.; Cheng, D.; Li, H.; Yu, J.; Wang, Q.; Gao, H.; Guo, J.; Wang, H.; Ozin, G. A.; Wang, T.; Gong, J. Efficient CO2 Electroreduction on Facet-Selective Copper Films with High Conversion Rate. *Nat. Commun.* **2021**, *12* (1), 5745. https://doi.org/10.1038/s41467-021-26053-w.

(16) Moura de Salles Pupo, M.; Kortlever, R. Electrolyte Effects on the Electrochemical Reduction of CO2. *ChemPhysChem* **2019**, *20* (22), 2926–2935. https://doi.org/10.1002/cphc.201900680.

(17) Varela, A. S.; Kroschel, M.; Reier, T.; Strasser, P. Controlling the Selectivity of CO2 Electroreduction on Copper: The Effect of the Electrolyte Concentration and the Importance of the Local pH. *Catal. Today* **2016**, *260*, 8–13. https://doi.org/10.1016/j.cattod.2015.06.009.

(18) Bui, J. C.; Kim, C.; King, A. J.; Romiluyi, O.; Kusoglu, A.; Weber, A. Z.; Bell, A. T. Engineering Catalyst–Electrolyte Microenvironments to Optimize the Activity and Selectivity for the Electrochemical Reduction of CO2 on Cu and Ag. *Acc. Chem. Res.* **2022**, *55* (4), 484–494. https://doi.org/10.1021/acs.accounts.1c00650.

(19) Loiudice, A.; Lobaccaro, P.; Kamali, E. A.; Thao, T.; Huang, B. H.; Ager, J. W.; Buonsanti, R. Tailoring Copper Nanocrystals towards C2 Products in Electrochemical CO2 Reduction. *Angew. Chem. Int. Ed.* **2016**, *55* (19), 5789–5792. https://doi.org/10.1002/anie.201601582.

(20) Mistry, H.; Varela, A. S.; Bonifacio, C. S.; Zegkinoglou, I.; Sinev, I.; Choi, Y.-W.; Kisslinger, K.; Stach, E. A.; Yang, J. C.; Strasser, P.; Cuenya, B. R. Highly Selective Plasma-Activated Copper Catalysts for Carbon Dioxide Reduction to Ethylene. *Nat. Commun.* **2016**, *7* (1), 12123. https://doi.org/10.1038/ncomms12123.

(21) National Renewable Energy Laboratory. *Typical Meteorological Year*. NSRDB: National Solar Radiation Database. https://nsrdb.nrel.gov/ (accessed 2023-09-20).

(22) Löwe, A.; Rieg, C.; Hierlemann, T.; Salas, N.; Kopljar, D.; Wagner, N.; Klemm, E. Influence of Temperature on the Performance of Gas Diffusion Electrodes in the CO2 Reduction Reaction. *ChemElectroChem* **2019**, *6* (17), 4497–4506. https://doi.org/10.1002/celc.201900872.

(23) Laoun, B.; Khellaf, A.; Naceur, M. W.; Kannan, A. M. Modeling of Solar Photovoltaic-Polymer Electrolyte Membrane Electrolyzer Direct Coupling for Hydrogen Generation. *Int. J. Hydrog. Energy* **2016**, *41* (24), 10120–10135. https://doi.org/10.1016/j.ijhydene.2016.05.041.

(24) Ben-Naim, M.; Aldridge, C. W.; Steiner, M. A.; Nielander, A. C.; Deustch, T. G.; Young, J. L.; Jaramillo, T. F. Demonstration of Photoreactor Platform for On-Sun Unassisted Photoelectrochemical Hydrogen Generation with Tandem III–V Photoelectrodes. *Chem Catal.* **2022**, *2* (1), 195–209. https://doi.org/10.1016/j.checat.2021.12.013.

(25) Lin, J.-A.; Roh, I.; Yang, P. Photochemical Diodes for Simultaneous Bias-Free Glycerol Valorization and Hydrogen Evolution. *J. Am. Chem. Soc.* **2023**, *145* (24), 12987–12991. https://doi.org/10.1021/jacs.3c01982.

(26) Holmes-Gentle, I.; Tembhurne, S.; Suter, C.; Haussener, S. Kilowatt-Scale Solar Hydrogen Production System Using a Concentrated Integrated Photoelectrochemical Device. *Nat. Energy* **2023**, *8* (6), 586–596. https://doi.org/10.1038/s41560-023-01247-2.

(27) Stevens, J. C.; Weber, A. Z. A Computational Study of Optically Concentrating, Solar-Fuels Generators from Annual Thermal- and Fuel-Production Efficiency Perspectives. *J. Electrochem. Soc.* **2016**, *163* (7), H475. https://doi.org/10.1149/2.0121607jes.

(28) Cheng, W.-H.; Richter, M. H.; Sullivan, I.; Larson, D. M.; Xiang, C.; Brunschwig, B. S.; Atwater, H. A. CO_2 Reduction to CO with 19% Efficiency in a Solar-Driven Gas Diffusion Electrode Flow Cell under Outdoor Solar Illumination. *ACS Energy Lett.* **2020**, *5* (2), 470–476. https://doi.org/10.1021/acsenergylett.9b02576.

(29) Greenblatt, J. B.; Miller, D. J.; Ager, J. W.; Houle, F. A.; Sharp, I. D. The Technical and Energetic Challenges of Separating (Photo)Electrochemical Carbon Dioxide Reduction Products. *Joule* **2018**, *2* (3), 381–420. https://doi.org/10.1016/j.joule.2018.01.014.

(30) Kim, J.; Jeong, S.; Beak, M.; Park, J.; Kwon, K. Performance of Photovoltaic-Driven Electrochemical Cell Systems for CO_2 Reduction. *Chem. Eng. J.* **2022**, *428*, 130259. https://doi.org/10.1016/j.cej.2021.130259.

(31) Wei, W. J.; King, A. J.; Bui, J. C.; Weber, A. Z.; Bell, A. T. Co-Design of Multijunction Photoelectrochemical Devices for Unassisted CO_2 Reduction to Multicarbon Products. *J. Electrochem. Soc.* **2023**, *170* (12), 126502. https://doi.org/10.1149/1945-7111/ad10e7.

(32) Yap, K. M. K.; Lee, S.-W.; Steiner, M. A.; Avilés Acosta, J. E.; Kang, D.; Kim, D.; Warren, E. L.; Nielander, A. C.; Jaramillo, T. F. A Framework for Understanding Efficient Diurnal CO_2 Reduction Using Si and GaAs Photocathodes. *Chem Catal.* **2023**, *3* (6), 100641. https://doi.org/10.1016/j.checat.2023.100641.

(33) Samu, A. A.; Kormányos, A.; Kecsenovity, E.; Szilágyi, N.; Endrődi, B.; Janáky, C. Intermittent Operation of CO_2 Electrolyzers at Industrially Relevant Current Densities. *ACS Energy Lett.* **2022**, *7* (5), 1859–1861. https://doi.org/10.1021/acsenergylett.2c00923.

(34) Edwards, J. P.; Alerte, T.; O'Brien, C. P.; Gabardo, C. M.; Liu, S.; Wicks, J.; Gaona, A.; Abed, J.; Xiao, Y. C.; Young, D.; Sedighian Rasouli, A.; Sarkar, A.; Jaffer, S. A.; MacLean, H. L.; Sargent, E. H.; Sinton, D. Pilot-Scale CO_2 Electrolysis Enables a Semi-Empirical Electrolyzer Model. *ACS Energy Lett.* **2023**, *8* (6), 2576–2584. https://doi.org/10.1021/acsenergylett.3c00620.

(35) Wang, Y.; Shen, H.; Livi, K. J. T.; Raciti, D.; Zong, H.; Gregg, J.; Onadeko, M.; Wan, Y.; Watson, A.; Wang, C. Copper Nanocubes for CO_2 Reduction in Gas Diffusion Electrodes. *Nano Lett.* **2019**, *19* (12), 8461–8468. https://doi.org/10.1021/acs.nanolett.9b02748.

(36) Zhang, J.; Luo, W.; Züttel, A. Self-Supported Copper-Based Gas Diffusion Electrodes for CO_2 Electrochemical Reduction. *J. Mater. Chem. A* **2019**, *7* (46), 26285–26292. https://doi.org/10.1039/C9TA06736A.

(37) N. Nguyen, T.; Dinh, C.-T. Gas Diffusion Electrode Design for Electrochemical Carbon Dioxide Reduction. *Chem. Soc. Rev.* **2020**, *49* (21), 7488–7504. https://doi.org/10.1039/D0CS00230E.

(38) Nielander, A. C.; Shaner, M. R.; Papadantonakis, K. M.; Francis, S. A.; Lewis, N. S. A Taxonomy for Solar Fuels Generators. *Energy Environ. Sci.* **2014**, *8* (1), 16–25. https://doi.org/10.1039/C4EE02251C.

(39) Choi, Y.; Song, J. Review of Photovoltaic and Wind Power Systems Utilized in the Mining Industry. *Renew. Sustain. Energy Rev.* **2017**, *75*, 1386–1391. https://doi.org/10.1016/j.rser.2016.11.127.

(40) Celik, I.; Lunardi, M.; Frederickson, A.; Corkish, R. Sustainable End of Life Management of Crystalline Silicon and Thin Film Solar Photovoltaic Waste: The Impact of Transportation. *Appl. Sci.* **2020**, *10* (16), 5465. https://doi.org/10.3390/app10165465.

(41) Holmgren, W. F.; Hansen, C. W.; Mikofski, M. A. Pvlib Python: A Python Package for Modeling Solar Energy Systems. *J. Open Source Softw.* **2018**, *3* (29), 884. https://doi.org/10.21105/joss.00884.

(42) Faiman, D. Assessing the Outdoor Operating Temperature of Photovoltaic Modules. *Prog. Photovolt. Res. Appl.* **2008**, *16* (4), 307–315. https://doi.org/10.1002/pip.813.

(43) *Global ethylene market size 2030*. Statista. https://www.statista.com/statistics/1349781/ethylene-global-market-size/ (accessed 2024-01-20).

(44) Mynko, O.; Amghizar, I.; Brown, D. J.; Chen, L.; Marin, G. B.; de Alvarenga, R. F.; Uslu, D. C.; Dewulf, J.; Van Geem, K. M. Reducing CO2 Emissions of Existing Ethylene Plants: Evaluation of Different Revamp Strategies to Reduce Global CO2 Emission by 100 Million Tonnes. *J. Clean. Prod.* **2022**, *362*, 132127. https://doi.org/10.1016/j.jclepro.2022.132127.

(45) Badgett, A.; Xi, W.; Ruth, M. *The Potential for Electrons to Molecules Using Solar Energy*; 2021.

(46) Mandal, L.; Yang, K. R.; Motapothula, M. R.; Ren, D.; Lobaccaro, P.; Patra, A.; Sherburne, M.; Batista, V. S.; Yeo, B. S.; Ager, J. W.; Martin, J.; Venkatesan, T. Investigating the Role of Copper Oxide in Electrochemical CO2 Reduction in Real Time. *ACS Appl. Mater. Interfaces* **2018**, *10* (10), 8574–8584. https://doi.org/10.1021/acsami.7b15418.

(47) Raciti, D.; Wang, C. Recent Advances in CO2 Reduction Electrocatalysis on Copper. *ACS Energy Lett.* **2018**, *3* (7), 1545–1556. https://doi.org/10.1021/acsenergylett.8b00553.

(48) Le, M.; Ren, M.; Zhang, Z.; Sprunger, P. T.; Kurtz, R. L.; Flake, J. C. Electrochemical Reduction of CO2 to CH3OH at Copper Oxide Surfaces. *J. Electrochem. Soc.* **2011**, *158* (5), E45. https://doi.org/10.1149/1.3561636.

(49) Tang, W.; A. Peterson, A.; Sofia Varela, A.; P. Jovanov, Z.; Bech, L.; J. Durand, W.; Dahl, S.; K. Nørskov, J.; Chorkendorff, I. The Importance of Surface Morphology in Controlling the Selectivity of Polycrystalline Copper for CO2 Electroreduction. *Phys. Chem. Chem. Phys.* **2012**, *14* (1), 76–81. https://doi.org/10.1039/C1CP22700A.

(50) Simon, G. H.; Kley, C. S.; Roldan Cuenya, B. Potential-Dependent Morphology of Copper Catalysts During CO2 Electroreduction Revealed by In Situ Atomic Force Microscopy. *Angew. Chem. Int. Ed.* **2021**, *60* (5), 2561–2568. https://doi.org/10.1002/anie.202010449.

(51) King, A. J.; Bui, J. C.; Bell, A. T.; Weber, A. Z. Establishing the Role of Operating Potential and Mass Transfer in Multicarbon Product Generation for Photoelectrochemical CO2 Reduction Cells Using a Cu Catalyst. *ACS Energy Lett.* **2022**, *7* (8), 2694–2700. https://doi.org/10.1021/acsenergylett.2c01041.

(52) Greenstreet, M. R.; Mitchell, I. Integrating Projections. In *Hybrid Systems: Computation and Control*; Henzinger, T. A., Sastry, S., Eds.; Lecture Notes in Computer Science; Springer: Berlin, Heidelberg, 1998; pp 159–174. https://doi.org/10.1007/3-540-64358-3_38.

(53) Badosa, J.; Haeffelin, M.; Chepfer, H. Scales of Spatial and Temporal Variation of Solar Irradiance on Reunion Tropical Island. *Sol. Energy* **2013**, *88*, 42–56. https://doi.org/10.1016/j.solener.2012.11.007.

(54) Kaabeche, A.; Bakelli, Y. Renewable Hybrid System Size Optimization Considering Various Electrochemical Energy Storage Technologies. *Energy Convers. Manag.* **2019**, *193*, 162–175. https://doi.org/10.1016/j.enconman.2019.04.064.

(55) Winkler, M. T.; Cox, C. R.; Nocera, D. G.; Buonassisi, T. Modeling Integrated Photovoltaic–Electrochemical Devices Using Steady-State Equivalent Circuits. *Proc. Natl. Acad. Sci.* **2013**, *110* (12), E1076–E1082. https://doi.org/10.1073/pnas.1301532110.

(56) Tawalbeh, M.; Farooq, A.; Martis, R.; Al-Othman, A. Optimization Techniques for Electrochemical Devices for Hydrogen Production and Energy Storage Applications. *Int. J. Hydrog. Energy* **2023**. https://doi.org/10.1016/j.ijhydene.2023.06.264.

(57) Gabardo, C. M.; O'Brien, C. P.; Edwards, J. P.; McCallum, C.; Xu, Y.; Dinh, C.-T.; Li, J.; Sargent, E. H.; Sinton, D. Continuous Carbon Dioxide Electroreduction to Concentrated Multi-Carbon Products Using a Membrane Electrode Assembly. *Joule* **2019**, *3* (11), 2777–2791. https://doi.org/10.1016/j.joule.2019.07.021.

(58) Goldman, M.; Prajapati, A.; Duoss, E.; Baker, S.; Hahn, C. Bridging Fundamental Science and Applied Science to Accelerate CO2 Electrolyzer Scale-Up. *Curr. Opin. Electrochem.* **2023**, *39*, 101248. https://doi.org/10.1016/j.coelec.2023.101248.

(59) Muroyama, A. P.; Pătru, A.; Gubler, L. Review—CO2 Separation and Transport via Electrochemical Methods. *J. Electrochem. Soc.* **2020**, *167* (13), 133504. https://doi.org/10.1149/1945-7111/abbbb9.

(60) Krödel, M.; Carter, B. M.; Rall, D.; Lohaus, J.; Wessling, M.; Miller, D. J. Rational Design of Ion Exchange Membrane Material Properties Limits the Crossover of CO2 Reduction Products in Artificial Photosynthesis Devices. *ACS Appl. Mater. Interfaces* **2020**, *12* (10), 12030–12042. https://doi.org/10.1021/acsami.9b21415.

(61) Ma, M.; Clark, E. L.; Therkildsen, K. T.; Dalsgaard, S.; Chorkendorff, I.; Seger, B. Insights into the Carbon Balance for CO2 Electroreduction on Cu Using Gas Diffusion Electrode Reactor Designs. *Energy Environ. Sci.* **2020**, *13* (3), 977–985. https://doi.org/10.1039/D0EE00047G.

(62) Nie, X.; Esopi, M. R.; Janik, M. J.; Asthagiri, A. Selectivity of CO2 Reduction on Copper Electrodes: The Role of the Kinetics of Elementary Steps. *Angew. Chem.* **2013**, *125* (9), 2519–2522. https://doi.org/10.1002/ange.201208320.

(63) Kortlever, R.; Shen, J.; Schouten, K. J. P.; Calle-Vallejo, F.; Koper, M. T. M. Catalysts and Reaction Pathways for the Electrochemical Reduction of Carbon Dioxide. *J. Phys. Chem. Lett.* **2015**, *6* (20), 4073–4082. https://doi.org/10.1021/acs.jpclett.5b01559.

(64) Gu, Z.; Shen, H.; Shang, L.; Lv, X.; Qian, L.; Zheng, G. Nanostructured Copper-Based Electrocatalysts for CO2 Reduction. *Small Methods* **2018**, *2* (11), 1800121. https://doi.org/10.1002/smtd.201800121.

(65) Haussener, S.; Hu, S.; Xiang, C.; Weber, A. Z.; Lewis, N. S. Simulations of the Irradiation and Temperature Dependence of the Efficiency of Tandem Photoelectrochemical Water-Splitting Systems. *Energy Environ. Sci.* **2013**, *6* (12), 3605–3618. https://doi.org/10.1039/C3EE41302K.

(66) Gattrell, M.; Gupta, N.; Co, A. A Review of the Aqueous Electrochemical Reduction of CO2 to Hydrocarbons at Copper. *J. Electroanal. Chem.* **2006**, *594* (1), 1–19. https://doi.org/10.1016/j.jelechem.2006.05.013.

(67) Woldu, A. R.; Huang, Z.; Zhao, P.; Hu, L.; Astruc, D. Electrochemical CO2 Reduction (CO2RR) to Multi-Carbon Products over Copper-Based Catalysts. *Coord. Chem. Rev.* **2022**, *454*, 214340. https://doi.org/10.1016/j.ccr.2021.214340.

(68) Żogała, A. Equilibrium Simulations of Coal Gasification – Factors Affecting Syngas Composition. *J. Sustain. Min.* **2014**, *13* (2), 30–38. https://doi.org/10.7424/jsm140205.

(69) Adnan, M. A.; Hidayat, A.; Hossain, M. M.; Muraza, O. Transformation of Low-Rank Coal to Clean Syngas and Power via Thermochemical Route. *Energy* **2021**, *236*, 121505. https://doi.org/10.1016/j.energy.2021.121505.

(70) Li, X.; Anderson, P.; Jhong, H.-R. M.; Paster, M.; Stubbins, J. F.; Kenis, P. J. A. Greenhouse Gas Emissions, Energy Efficiency, and Cost of Synthetic Fuel Production Using Electrochemical CO2 Conversion and the Fischer–Tropsch Process. *Energy Fuels* **2016**, *30* (7), 5980–5989. https://doi.org/10.1021/acs.energyfuels.6b00665.

(71) Choi, M.; Kim, J. W.; Chung, S.; Lee, Y.; Bong, S.; Lee, J. Syngas Production for Fischer-Tropsch Process via Co-Electrolytic Processes of CO2 Reduction and NH3 Oxidation. *Chem. Eng. J.* **2022**, *430*, 132563. https://doi.org/10.1016/j.cej.2021.132563.

(72) Küngas, R. Review—Electrochemical CO2 Reduction for CO Production: Comparison of Low- and High-Temperature Electrolysis Technologies. *J. Electrochem. Soc.* **2020**, *167* (4), 044508. https://doi.org/10.1149/1945-7111/ab7099.

(73) Allebrod, F.; Chatzichristodoulou, C.; Mollerup, P. L.; Mogensen, M. B. Electrical Conductivity Measurements of Aqueous and Immobilized Potassium Hydroxide. *Int. J. Hydrog. Energy* **2012**, *37* (21), 16505–16514. https://doi.org/10.1016/j.ijhydene.2012.02.088.

(74) See, D. M.; White, R. E. Temperature and Concentration Dependence of the Specific Conductivity of Concentrated Solutions of Potassium Hydroxide. *J. Chem. Eng. Data* **1997**, *42* (6), 1266–1268. https://doi.org/10.1021/je970140x.

(75) Weng, L.-C.; Bell, A. T.; Weber, A. Z. A Systematic Analysis of Cu-Based Membrane-Electrode Assemblies for CO2 Reduction through Multiphysics Simulation. *Energy Environ. Sci.* **2020**, *13* (10), 3592–3606. https://doi.org/10.1039/D0EE01604G.

(76) Applebaum, J. The Quality of Load Matching in a Direct-Coupling Photovoltaic System. *IEEE Trans. Energy Convers.* **1987**, *EC-2* (4), 534–541. https://doi.org/10.1109/TEC.1987.4765889.

(77) Teng, H.; Yamasaki, A. Mass Transfer of CO2 through Liquid CO2–Water Interface. *Int. J. Heat Mass Transf.* **1998**, *41* (24), 4315–4325. https://doi.org/10.1016/S0017-9310(98)00173-2.

(78) Luqmani, B.; Brookes, A.; Moore, A.; Vale, P.; Pidou, M.; McAdam, E. J. The Role of Solvent Temperature and Gas Pressure on CO2 Mass Transfer during Biogas Upgrading within Porous and Dense-Skin Hollow Fibre Membrane Contactors. *J. Membr. Sci.* **2023**, *685*, 121967. https://doi.org/10.1016/j.memsci.2023.121967.

(79) Song, W.; Liu, Y.; Wang, Z.; Ding, S.; Lin, X.; Feng, Z.; Li, Z. A Novel Wind Turbine Control Strategy to Maximize Load Capacity in Severe Wind Conditions. *Energy Rep.* **2022**, *8*, 7773–7779. https://doi.org/10.1016/j.egyr.2022.06.005.

(80) Popović, S.; Smiljanić, M.; Jovanovič, P.; Vavra, J.; Buonsanti, R.; Hodnik, N. Stability and Degradation Mechanisms of Copper-Based Catalysts for Electrochemical CO2 Reduction. *Angew. Chem.* **2020**, *132* (35), 14844–14854. https://doi.org/10.1002/ange.202000617.

(81) Dinh, C.-T.; Burdyny, T.; Kibria, M. G.; Seifitokaldani, A.; Gabardo, C. M.; García de Arquer, F. P.; Kiani, A.; Edwards, J. P.; De Luna, P.; Bushuyev, O. S.; Zou, C.; Quintero-Bermudez, R.; Pang, Y.; Sinton, D.; Sargent, E. H. CO2 Electroreduction to Ethylene via Hydroxide-Mediated Copper Catalysis at an Abrupt Interface. *Science* **2018**, *360* (6390), 783–787. https://doi.org/10.1126/science.aas9100.

(82) Ni, W.; Li, C.; Zang, X.; Xu, M.; Huo, S.; Liu, M.; Yang, Z.; Yan, Y.-M. Efficient Electrocatalytic Reduction of CO2 on CuxO Decorated Graphene Oxides: An Insight into the Role of Multivalent Cu in Selectivity and Durability. *Appl. Catal. B Environ.* **2019**, *259*, 118044. https://doi.org/10.1016/j.apcatb.2019.118044.

(83) Lai, W.; Qiao, Y.; Wang, Y.; Huang, H. Stability Issues in Electrochemical CO2 Reduction: Recent Advances in Fundamental Understanding and Design Strategies. *Adv. Mater.* **2023**, *35* (51), 2306288. https://doi.org/10.1002/adma.202306288.

(84) Sánchez, M.; Amores, E.; Rodríguez, L.; Clemente-Jul, C. Semi-Empirical Model and Experimental Validation for the Performance Evaluation of a 15 kW Alkaline Water Electrolyzer. *Int. J. Hydrog. Energy* **2018**, *43* (45), 20332–20345. https://doi.org/10.1016/j.ijhydene.2018.09.029.

(85) Santarelli, M.; Medina, P.; Calì, M. Fitting Regression Model and Experimental Validation for a High-Pressure PEM Electrolyzer. *Int. J. Hydrog. Energy* **2009**, *34* (6), 2519–2530. https://doi.org/10.1016/j.ijhydene.2008.11.036.

(86) Ojong, E. T.; Kwan, J. T. H.; Nouri-Khorasani, A.; Bonakdarpour, A.; Wilkinson, D. P.; Smolinka, T. Development of an Experimentally Validated Semi-Empirical Fully-Coupled Performance Model of a PEM Electrolysis Cell with a 3-D Structured Porous Transport Layer. *Int. J. Hydrog. Energy* **2017**, *42* (41), 25831–25847. https://doi.org/10.1016/j.ijhydene.2017.08.183.

(87) Çıtmacı, B.; Luo, J.; Jang, J. B.; Canuso, V.; Richard, D.; Ren, Y. M.; Morales-Guio, C. G.; Christofides, P. D. Machine Learning-Based Ethylene Concentration Estimation, Real-Time Optimization and Feedback Control of an Experimental Electrochemical Reactor. *Chem. Eng. Res. Des.* **2022**, *185*, 87–107. https://doi.org/10.1016/j.cherd.2022.06.044.

(88) Shockley, W.; Queisser, H. J. Detailed Balance Limit of Efficiency of P-n Junction Solar Cells. *J. Appl. Phys.* **1961**, *32* (3), 510–519. https://doi.org/10.1063/1.1736034.

(89) Chen, Y.; Lewis, N. S.; Xiang, C. Modeling and Simulation of the Spatial and Light-Intensity Dependence of Product Distributions in an Integrated Photoelectrochemical CO2 Reduction System. *ACS Energy Lett.* **2016**, *1* (1), 273–280. https://doi.org/10.1021/acsenergylett.6b00134.

(90) Sze, S. M.; Ng, K. K. *Physics of Semiconductor Devices*, 3rd ed.; John Wiley & Sons, Ltd, 2006. https://doi.org/10.1002/0470068329.

(91) Blakers, A. W.; Green, M. A. 678-mV Open-circuit Voltage Silicon Solar Cells. *Appl. Phys. Lett.* **1981**, *39* (6), 483–485. https://doi.org/10.1063/1.92767.

(92) Zanatta, A. R. The Shockley–Queisser Limit and the Conversion Efficiency of Silicon-Based Solar Cells. *Results Opt.* **2022**, *9*, 100320. https://doi.org/10.1016/j.rio.2022.100320.